AIAA JOURNAL
Vol. 47, No. 12, December 2009

Numerical Investigation of Broadband Slat Noise Attenuation with Acoustic Liner Treatment

Zhaokai Ma* and Xin Zhang†
University of Southampton, Southampton, England SO17 1BJ United Kingdom

DOI: 10.2514/1.39883

The acoustic field produced by broadband noise sources around the slat of a high-lift wing model is predicted using a hybrid method based on a large eddy simulation of the compressible flow for the noise generation and acoustic perturbation equation calculations for the acoustic propagation. The potential for noise attenuation using acoustic liners within the slat gap region of the high-lift wing is investigated by solving the acoustic perturbation equations with a broadband time-domain impedance boundary condition, and the acoustic liner conditions are applied on the slat cove surface and the main element. Results show that attenuation of the broadband noise is obtained with the acoustic liner treatment in the slat gap region.

Nomenclature

Att	=	acoustic attenuation
C	=	high-lift wing chord length
C_s	=	slat chord length
c	=	sound speed
d	=	nondimensionalized distance from the wall
$\hat{\mathbf{F}}$, $\hat{\mathbf{G}}$, and $\hat{\mathbf{H}}$	=	inviscid fluxes of Navier–Stokes equations
$\hat{\mathbf{F}}_v$, $\hat{\mathbf{G}}_v$, and $\hat{\mathbf{H}}_v$	=	viscous fluxes of Navier–Stokes equations
f	=	frequency
L	=	characteristic length
$\mathbf{L}$, $\mathbf{D}$, and $\mathbf{U}$	=	lower-upper factorization matrices
M	=	Mach number
p	=	static pressure
Q	=	vorticity criterion
$\hat{\mathbf{Q}}$	=	solution vector of Navier–Stokes equations
q_c	=	mass source term of acoustic perturbation equations
$\mathbf{q}_m$	=	momentum source term vector of acoustic perturbation equations
R	=	acoustic resistance
Re_L	=	Reynolds number based on a characteristic length L
S_{ij}	=	symmetric components of $\nabla\mathbf{u}$
St	=	Strouhal number
s	=	distance along the observed circle
t	=	time
$\mathbf{u}$	=	Cartesian velocity vector
u, v, and w	=	Cartesian velocity components
X	=	acoustic reactance
X_1	=	modeled acoustic mass
X_{-1}	=	modeled acoustic stiffness
x, y, and z	=	Cartesian coordinates
Z	=	acoustic impedance
ξ, η, and ζ	=	generalized coordinates
ρ	=	fluid density
$\hat{\phi}_f$	=	Fourier transform coefficient at frequency f
Ω_{ij}	=	antisymmetric components of $\nabla\mathbf{u}$
ω	=	vorticity

Superscript

$()'$	=	perturbation value

Subscripts

$()_{\mathrm{RMS}}$	=	root mean square value
$()_0$	=	time-averaged value
$()_\infty$	=	freestream value

I. Introduction

WITH the development of low-noise high-bypass engine, airframe noise has become an important component of the overall aircraft noise source (especially during approach to the landing phase of the aircraft operation). Airframe noise is mainly generated by flap side edges, slats, and landing gear. The spectrum of the slat noise can contain both tonal and broadband components. The tonal noise generation mechanism has been widely investigated [1–3]. Potential attenuation methods for the tonal slat noise include perforated materials [4], serrated tapes [5], and acoustic liners [6]. All the treatments give a significant reduction of the tonal slat noise. Specifically, the liner treatment [6] is shown to be effective in attenuating the tonal noise generated at the trailing edge of the slat. The attenuation of the broadband noise using acoustic liners is more challenging, although the experiment of Smith et al. [7] shows encouraging results. The directivity of the slat noise source and its propagation characteristics through the lined slat gap is a complex function of frequency, flow, and slat geometry. This creates problems for experimentation at model scale and a good reason for developing some understanding through the use of numerical models. The objective of this work is to investigate the performance of acoustic liners for broadband slat noise reduction with large eddy simulation (LES)/acoustic perturbation equation (APE) hybrid computations.

The generation of the broadband slat noise represents a complex aeroacoustic problem that involves the vortex generation from the slat cusp, the vortex breakdown, and the vortex distortion near the reattachment point [8]. To understand the physics and mechanisms behind these phenomena and find a way to reduce the overall slat noise, accurate simulations (for example, LES or detached eddy simulation) of the complex unsteadiness flow of a high-lift wing are needed. In the past, a hybrid Reynolds averaged Navier–Stokes (RANS)/LES method was attempted in which the LES zone was confined in the slat cove region [9]. A zonal-detached-eddy simulation of the flow around a high-lift configuration shows good agreement between the computed and measured mean flows [10].

Presented as Paper 2964 at the 14th AIAA/CEAS Aeroacoustics Conference, Vancouver, British Columbia, Canada, 5–7 May 2008; received 20 July 2008; revision received 11 July 2009; accepted for publication 11 July 2009.

*Research Fellow, Aeronautics and Astronautics; mazhk@soton.ac.uk. Member AIAA.

†Professor, Aeronautics and Astronautics; xzhang@soton.ac.uk. Associate Fellow AIAA.

The calculation captures the important unsteadiness in the slat cove, such as roll up and formation of discrete vortices. Another method to predict the broadband slat noise is the pseudolaminar zonal method proposed by Khorrami et al. [11]. In this method (based on the knowledge that the flow in the slat cove region is in low velocity and behaves in a quasi-laminar manner), the slat cove region is treated as a laminar zone, whereas other regions of the flow are treated as fully turbulent regions. Khorrami et al. compared the numerical prediction with experiment data [8,12] and suggested that the pseudolaminar zonal method produces good results in terms of broadband noise spectrum.

For broadband noise prediction, the stochastic noise generation approach can also be a low-cost alternative [13–17]. The advantage of this method is that only a steady RANS calculation is needed in order to obtain the broadband noise sources. After the turbulent kinetic energy and turbulent dissipation rate are calculated by a RANS simulation, the perturbation velocity can be realized either by the sum of random Fourier modes [13] or by the application of solenoidal digital filters [17]. The broadband noise sources calculated from the perturbation velocity field can then be used as source terms in linearized Euler equations to simulate the acoustic field. The applications of this approach to jet noise [13–15], trailing edge noise [16], and slat noise [17] predictions show that it can be an effective tool to perform parameter studies.

A frequency domain method was also developed to predict the broadband slat noise [18]. In this method, the broadband noise emanating from the cove region of a slat is predicted using a two-step process. First, the noise sources are modeled based on amplitude, length, and time scales obtained from a RANS calculated turbulence field and at least one experimental measurement of the noise spectrum. Then, the sound from these sources is propagated by a convected wave equation. A Green's function for the convected wave equation is derived to take into account the scattering effects of the high-lift wing in the presence of a uniform background mean flow, which is solved by a boundary element method. Once the Green's function and noise source terms are known, the final noise prediction is obtained by forming a convolution of Green's function with modeled noise sources.

In this work, the acoustic field of a high-lift wing model with a deployed slat is investigated by a hybrid method. First, the broadband noise generation process is simulated using LES, and then the acoustic field is calculated by solving APE [19] with the source terms obtained from LES. The broadband noise attenuation potential of the acoustic liner treatment is studied by applying a broadband time-domain impedance boundary condition [20] to the slat cove surface and the leading edge of the main element in the APE computations. Furthermore, the far-field directivity of cases with and without the acoustic liner treatment is obtained through integral surface solutions of the Ffowcs Williams and Hawkings (FW–H) equation, which is a rearrangement of the Navier–Stokes equations into the form of an inhomogeneous wave equation [21].

The rest of the paper is organized as follows. The numerical methods used in the simulations are described in Sec. II. In Sec. III, the results of the broadband slat noise generation and propagation are presented, and the effects of the acoustic liner treatment on the slat and the main element are discussed. Finally, conclusions are given in Sec. IV.

II. Numerical Methods

A. Large Eddy Simulation Solver

The governing equations of the LES solver are the unsteady three-dimensional (3-D) compressible Favre-filtered Navier–Stokes equations. In the absence of body forces and external heat addition, these equations can be written as follows:

$$\frac{\partial \hat{\mathbf{Q}}}{\partial t}+\frac{\partial \hat{\mathbf{F}}}{\partial \xi}+\frac{\partial \hat{\mathbf{G}}}{\partial \eta}+\frac{\partial \hat{\mathbf{H}}}{\partial \zeta}=\frac{M_\infty}{Re_L}\left[\frac{\partial \hat{\mathbf{F}}_v}{\partial \xi}+\frac{\partial \hat{\mathbf{G}}_v}{\partial \eta}+\frac{\partial \hat{\mathbf{H}}_v}{\partial \zeta}\right] \tag{1}$$

where t is the time; ξ, η, and ζ are the computational coordinates; $\hat{\mathbf{Q}}$ denotes the solution vector; $\hat{\mathbf{F}}$, $\hat{\mathbf{G}}$, and $\hat{\mathbf{H}}$ are the inviscid flux vectors, and $\hat{\mathbf{F}}_v$, $\hat{\mathbf{G}}_v$, and $\hat{\mathbf{H}}_v$ are the viscous flux vectors [22]. M_∞ is the Mach number of the freestream flow and Re_L is the Reynolds number based on the freestream velocity and the characteristic length L. The subgrid-stress model used in the simulation is the Smagorinsky model [23].

The governing equations are solved by an implicit lower–upper (LU) approximate factorization algorithm [24] employing Newton-like subiterations that can be written as

$$\begin{aligned}(\mathbf{L}+\mathbf{D})\mathbf{D}^{-1}(\mathbf{D}+\mathbf{U})\Delta\hat{\mathbf{Q}}^m=&-\frac{3\hat{\mathbf{Q}}^m-4\hat{\mathbf{Q}}^n+\hat{\mathbf{Q}}^{n-1}}{2}\\&-\Delta t D_{\xi 6}\left(\hat{\mathbf{F}}^m-\frac{M_\infty}{Re_L}\hat{\mathbf{F}}_v^m\right)-\Delta t D_{\eta 6}\left(\hat{\mathbf{G}}^m-\frac{M_\infty}{Re_L}\hat{\mathbf{G}}_v^m\right)\\&-\Delta t D_{\zeta 6}\left(\hat{\mathbf{H}}^m-\frac{M_\infty}{Re_L}\hat{\mathbf{H}}_v^m\right)\end{aligned} \tag{2}$$

where the $D_{\xi 6}$, $D_{\eta 6}$, and $D_{\zeta 6}$ represent the sixth-order difference in the ξ, η, and ζ directions (respectively) and $\mathbf{L}$, $\mathbf{D}$, and $\mathbf{U}$ are the LU factorization matrices [24].

In the expression, a first-order backward difference formula is used to discretize the pseudotime derivative, and a second-order backward difference formula is used to discretize the physical time derivative. The implicit segment of the algorithm incorporates a second-order spatial difference, and the explicit segment of the algorithm is evaluated using the sixth-order compact scheme [25] combined with a tenth-order nondispersive filter [26]. To achieve second-order temporal accuracy, subiterations are used to reduce the errors due to factorization, linearization, and the explicit implementation of the boundary condition. In Eq. (2), $\hat{\mathbf{Q}}^{m+1}$ is the $m+1$ subiteration to approximate $\hat{\mathbf{Q}}$ at the $n+1$ time level and $\Delta\hat{\mathbf{Q}}=\hat{\mathbf{Q}}^{m+1}-\hat{\mathbf{Q}}^m$. At time level n, the solution is advanced from $m=1$ and $\hat{\mathbf{Q}}^m=\hat{\mathbf{Q}}^n$. Three to five subiterations per time step are found to be suitable for flow calculation [22,27,28].

B. Acoustic Solver

For the near-field acoustic propagation calculation, the APE proposed by Ewert and Schröder [19] are adopted:

$$\begin{aligned}\frac{\partial \rho'}{\partial t}+\nabla(\rho_0\mathbf{u}'+\mathbf{u}_0\rho')&=q_c\\\frac{\partial \mathbf{u}'}{\partial t}+\nabla(\mathbf{u}_0\cdot\mathbf{u}')+\nabla\left(\frac{p'}{\rho_0}\right)&=\mathbf{q_m}\end{aligned} \tag{3}$$

where ρ is density, p is pressure, and $\mathbf{u}$ is the velocity vector. Subscript $(\,)_0$ denotes the time-averaged mean value, and the prime sign denotes the perturbation value. The q_c and $\mathbf{q}_m$ are the mass source term and momentum source term vector of the APE, respectively. Based on the definition of the APE-4 system [19], and by ignoring the viscous term, the nonlinear term, and the entropy term, the resulted source terms can be written as

$$q_c=0; \qquad \mathbf{q_m}=-(\omega\times\mathbf{u})' \tag{4}$$

where $\omega=\nabla\times\mathbf{u}$.

The APE is solved using an optimized prefactored compact scheme [29] to evaluate the spatial derivative and a 4–6 low-dispersion and dissipation Runge–Kutta optimized scheme for the time integration [30].

To provide an assessment of the benefit of the acoustic liners, the far-field directivity is obtained by solving FW–H equations using formulation 1A of Farassat [21], in which the volume quadrupole terms are neglected.

III. Results and Discussion

A. Aerodynamic Flowfield

1. *Computation Setup*

The high-lift wing configuration investigated comprises a main element, a slat, and a flap. To reduce the number of grid points, the

slat is set in a deployed position and the flap is set in the retracted position in the LES calculation. The model has a chord length C of 0.8 m with the slat and flap in the retracted position, and the slat chord is 12% of the overall chord length. The freestream Mach number is 0.2, and the main element angle of attack (AOA) is 12 deg to represent the 5 deg AOA approaching condition in which the flap is in a deployed position. Previous work indicates that the 12 deg AOA configuration matches the 5 deg AOA configuration well in terms of the mean flow streamlines, the mean Mach contours, the trajectory shape of the shear layer, and the location of the reattachment point in the slat cove [28]. In this study, a Cartesian coordinates system is employed and x is in the horizontal direction, y is in the vertical direction, and z is in the spanwise direction. The velocity components in the x, y, and z directions are u, v, and w, respectively.

A 3-D grid for the LES is generated by uniformly extruding a basic two-dimensional (2-D) grid along the spanwise z direction. The basic 2-D grid consists of 144 blocks with a total of 210,000 nodes, and the total computational domain ranges from -10 to $10C$ in both the x and y directions (which are shown in Fig. 1). The grids are designed to ensure $y^+ = O(1)$ along all solid walls, and the boundary layers are resolved with a minimum of 30 mesh points. Following the recommendation by Spalart [31], the grid spacing in the spanwise direction is chosen as $0.002C$ so that in the LES region, the grids have similar sizes in all three dimensions. A total of 26 grid points are used in the spanwise direction, yielding a spanwise domain range from 0 to $0.05C$ and a total of 5.46 million points. The grid near the slat cove region is shown in Fig. 2. An explicit form of buffer zone boundary conditions [32] is used as the freestream boundary condition, and a periodic boundary condition is used in spanwise direction.

The computation is performed on a Linux cluster using 48 2.2 GHz Advanced Micro Devices (AMD) Opterons CPUs. The CPU cost per subiteration is 9.8 s, and the time step is fixed to $0.0001C/c_\infty$ with five Newton-like subiterations, yielding a maximum Courant–Friedrichs–Lewy (CFL) number based on an acoustic velocity $(u_\infty + c_\infty)$ equal to 15, where u_∞ and c_∞ are freestream velocity and sound speed, respectively. The time step corresponds to a sampling frequency of 4.25 MHz, and the flow-through time scale based on the chord of the slat and the freestream velocity corresponds to 6000 time steps. After the transient stage, the calculation is run over 30 slat flow-through time units to ensure good mean and statistic results.

Unless indicated otherwise, all the values in the rest of this section are shown in nondimensionalized form: all the length scales are nondimensionalized by C (which is the chord length of the wing with the slat and the flap retracted) and the velocities by c_∞. The density is nondimensionalized by ρ_∞ and the pressure by $\rho_\infty c_\infty^2$.

2. *Instantaneous Flow*

For the slat flow, the instantaneous vortical structures captured by the simulation are shown by the isosurfaces of the Q criterion [33], which is defined as

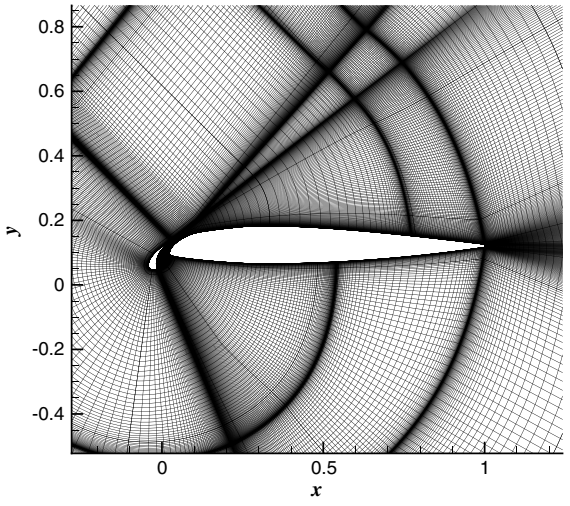

Fig. 1 A view of the cross section of the LES grid for the high-lift wing.

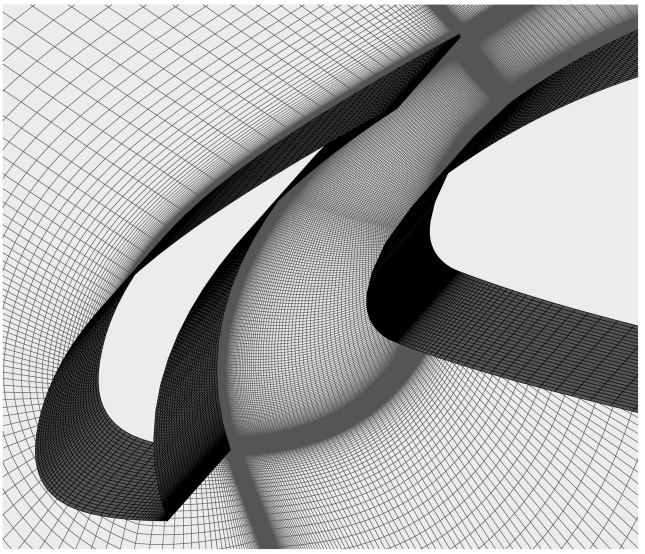

Fig. 2 A view of the LES grid in the slat cove region.

$$Q = \frac{1}{2}(\Omega_{ij}\Omega_{ij} - S_{ij}S_{ij}) = -\frac{1}{2}\frac{\partial u_i}{\partial x_j}\frac{\partial u_j}{\partial x_i} > 0 \tag{5}$$

where S_{ij} and Ω_{ij} are the symmetric and antisymmetric components of $\nabla\mathbf{u}$.

Figure 3 shows the vortical structures in the slat cove, in which the isosurfaces of Q colored with the z-direction vorticity ω_z are plotted. Large vortical structures are observed to shed from the slat cusp and are mainly 2-D structures in the early stages of their development. As these structures roll up toward the reattachment position on the cove surface of the slat, they show more 3-D character. Near the reattachment position, the vortical structures are distorted by the mean flow strain; some of these large structures are seen to pass through the slat gap and some of them are entrapped into the slat cove region, moving toward the cusp. The entrapped vortical structures induce a secondary separation on the slat cove surface, and the resulting secondary vortical structures are believed to be one of the causes of the rapid 3-D breakdown of the vortical structures in the shear layer [8].

Figure 4 presents plots of the z-direction vorticity on three different cross-sectional planes, for which L_z is the spanwise length of the computational domain. The results show the strong unsteadiness in the slat cove region. The calculated 3-D coherent vortical

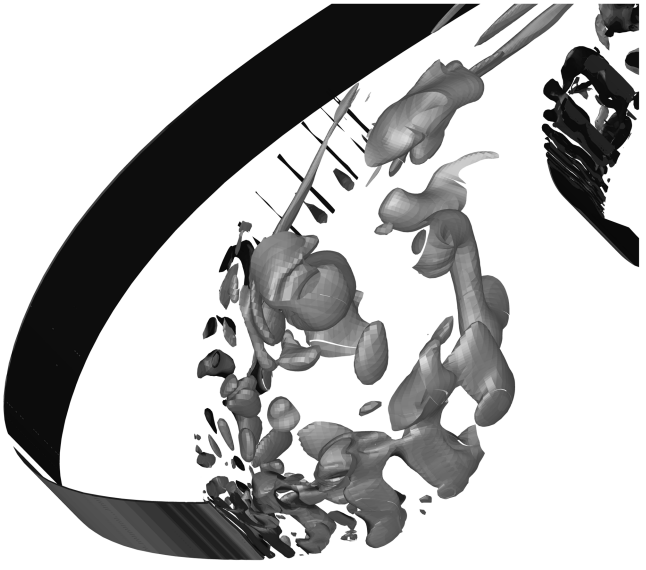

Fig. 3 Q isosurfaces colored with z-direction vorticity.

structures are consistent with the past particle image velocimetry (PIV) measurements [34–37] and other numerical simulations [8,10].

3. Time-Averaged Flow

The mean variables are averaged over the last 60,000 steps of the computation, which corresponds to 6 nondimensional time units or 10 slat flow-through time units. Figure 5 shows the streamlines of the mean flow and the mean Mach contours of the high-lift configuration. The acceleration of the flow through the slat and the main element gap and the slow speed recirculation zone are separated by a shear layer.

The locations of the monitoring lines are given in Fig. 6, and the profiles of the mean velocity magnitude $|\mathbf{u}_0|$ along two lines (line A and line B) in the slat cove are plotted in Fig. 7. In Fig. 7, the distance d is calculated from the slat cove surface and is nondimensionalized by the chord of the high-lift wing configuration. Along line A, the velocity magnitude first increases from zero as it departs from the nonslip wall. Then, in the recirculation region, the velocity magnitude decreases toward zero as it approaches the center of the recirculation region and increases again when it passes the center. In the shear layer, there is a significant velocity gradient; the velocity magnitude increases rapidly moving away from the cove surface and, out of the shear layer, the velocity decreases again. A similar trend is recorded on line B, except that the velocity magnitude keeps increasing out of the shear layer as the local flow is accelerated through the slat gap.

The time- and span-averaged z-direction vorticity in the slat cove region is shown in Fig. 8. The PIV measurements and the 3-D pseudolaminar computation results reported by Choudhari and Khorrami [8] show similar results, except the vorticity thickness is thinner in the 3-D pseudolaminar results.

4. Fluctuation Statistics

The fluctuation statistics of the flowfields give hints to the characteristics of the unsteadiness and the noise sources. The 2-D turbulent kinetic energy on the middle span cross section of the slat geometry is shown in Fig. 9. Here, the 2-D turbulent kinetic energy is defined as

$$\mathrm{TKE}_{2\mathrm{D}} = \tfrac{1}{2}(\overline{u'^2} + \overline{v'^2}) \tag{6}$$

where the overbar denotes the time average. The LES produces high 2-D turbulent kinetic energy values near the slat cusp and the reattachment position, and in the recirculation zone. The velocity fluctuations are monitored on line C (see Fig. 6) on the middle span cross section, as shown in Fig. 10. An examination of the root mean square (RMS) values of the different velocity components on line C indicate that the velocity component u has a nearly constant fluctuation level along the shear layer trajectory. The velocity component v has two peaks along the shear layer trajectory, for which one is near the slat cusp and the other is near the reattachment position. Along the most part of the trajectory, the w-velocity component has similar fluctuation levels to that of the u-velocity component (except near the reattachment position). The resulting

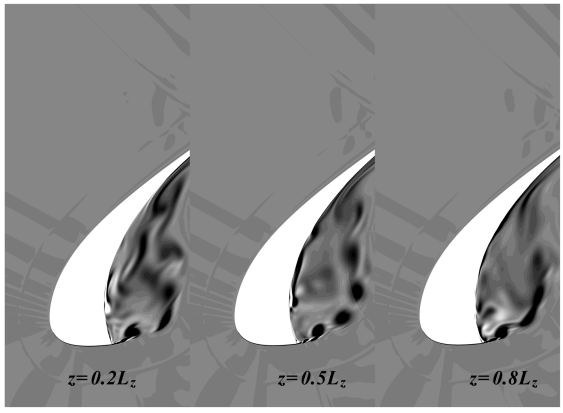

Fig. 4 Three different spanwise planes showing z-direction vorticity contours.

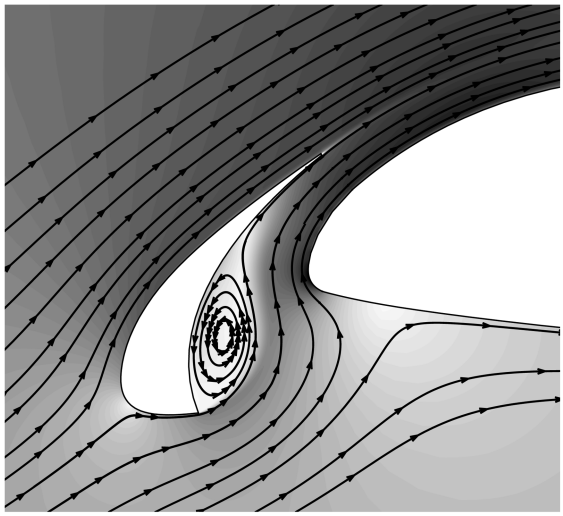

Fig. 5 A view of the mean flow streamlines near the slat.

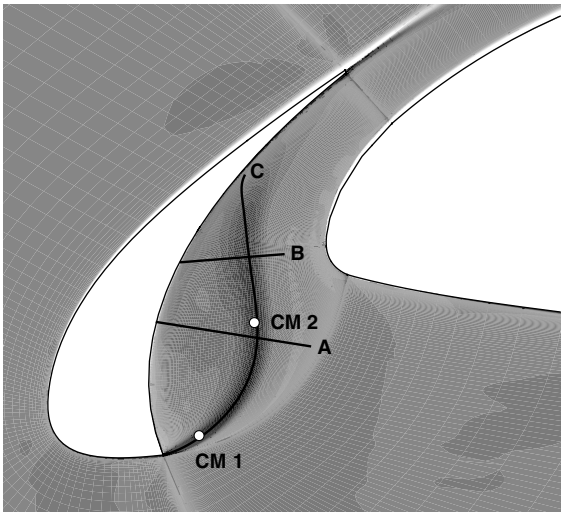

Fig. 6 Locations of the mixing layer profile monitoring lines.

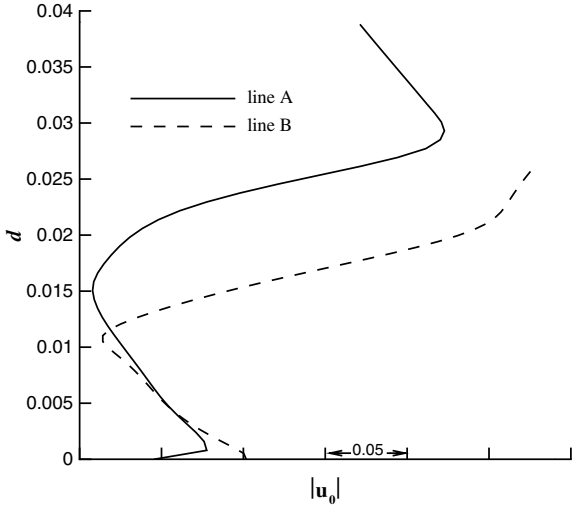

Fig. 7 Mean velocity profiles on the monitoring lines.

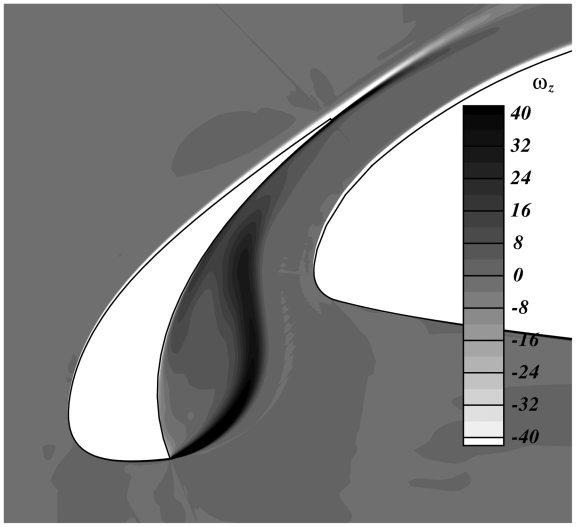

Fig. 8 Time-averaged z-direction vorticity in the slat cove region.

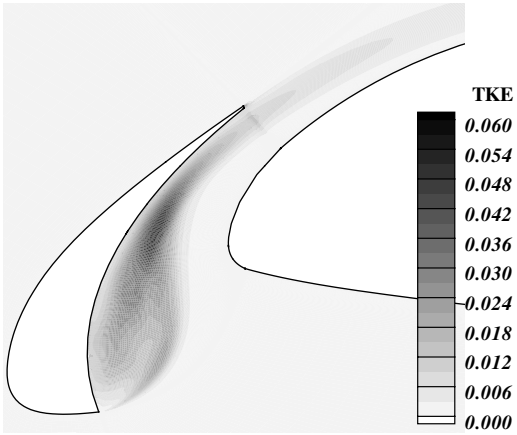

Fig. 9 Time-averaged turbulent kinetic energy in the slat cove region (TKE denotes turbulent kinetic energy).

3-D turbulent kinetic energy ($\mathrm{TKE_{3D}} = \frac{1}{2}(\overline{u'^2} + \overline{v'^2} + \overline{w'^2})$) therefore increases from the slat cusp to the first peak and then, near the reattachment point, it has two peaks. One is due to the large v-velocity fluctuation and the other is due to the large w-velocity fluctuation.

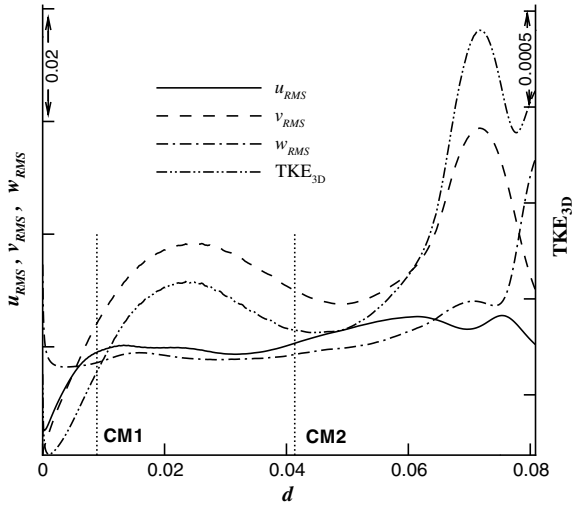

Fig. 10 3-D turbulent kinetic energy and velocity fluctuations along monitoring line C.

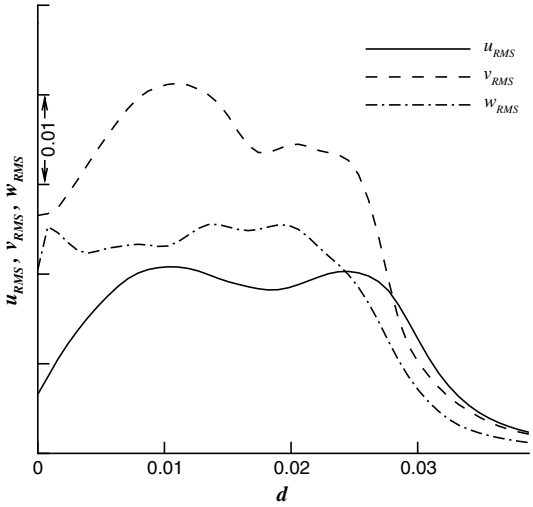

Fig. 11 Velocity fluctuations along monitoring line A.

The velocity component fluctuations inside the recirculation zone are monitored on line A, as shown in Fig. 11. The monitored results show a fully 3-D flow in the recirculation bubble. The u and w components have a peak fluctuation level of about 10% of the freestream velocity, and a higher peak value of 21% of the freestream velocity is observed for the v component. It should be noted that in the vicinity of the slat suction surface, the w has a relatively large value as the result of the 3-D secondary separation flow.

The spanwise correlations are monitored within the shear layer on the two lines CM1 and CM2, which are parallel to the z axis and start from the points with the Cartesian coordinates of (−0.0065, 0.05625, 0.024) and (0.007375, 0.085, 0.024), respectively (as shown in Fig. 6), in which the projections of the two lines on the x–y plane are shown as CM1 and CM2. The corresponding positions of CM1 and CM2 on line C are given in Fig. 10. Figures 12 and 13 show the correlation coefficients of the velocity component fluctuations along the spanwise direction, where R_{uu} is defined as

$$\overline{u'(x_0, y_0, z_0)u'(x_0, y_0, z)} / \overline{u'(x_0, y_0, z_0)u'(x_0, y_0, z_0)}$$

for a given staring point (x_0, y_0, z_0), and a similar definition applies to R_{vv} and R_{ww} where the overbar means the time average. The coefficients give rapid decreases in the spanwise direction, indicating that the spanwise grid size and the spanwise length used in the calculation are acceptable and the acoustic source coherence length is small compared with the chord length. It should be noted that

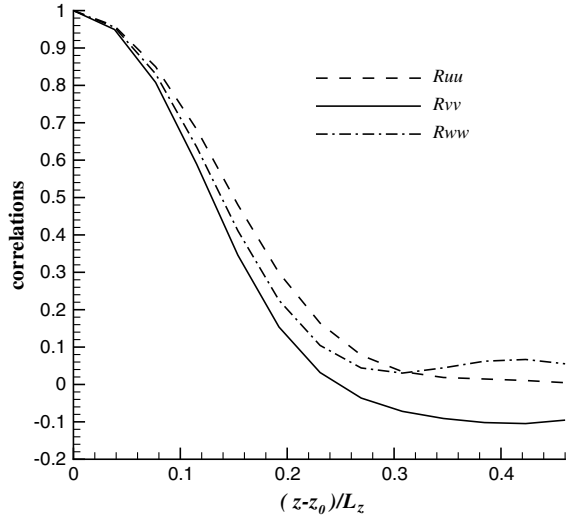

Fig. 12 Spanwise correlation of velocity perturbations on the monitoring line CM1.

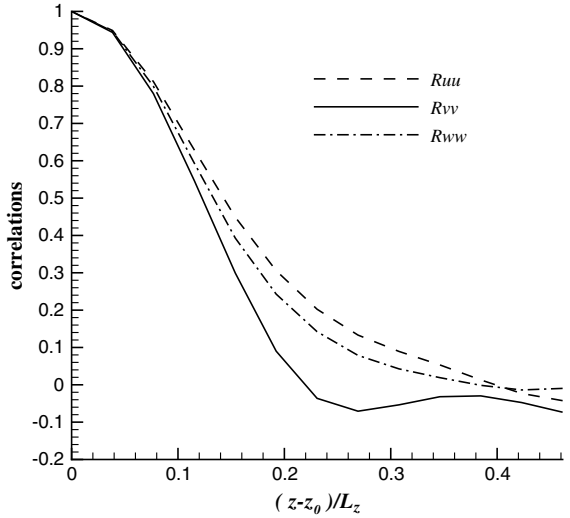

Fig. 13 Spanwise correlation of velocity perturbations on the monitoring line CM2.

additional computation with smaller spanwise grid size and larger spanwise length can resolve the smaller spanwise structures and describe the spanwise coherence more clearly.

The frequency spectra of the pressure perturbation at monitor position 1 (−0.0065, 0.05625, 0.024) and monitor position 2 (0.007375, 0.085, 0.024) are shown in Fig. 14, in which the ordinate corresponding to the frequency parameters times the power spectral densities (PSDs) [which is defined as $2|\hat{\phi}_f|^2/(t_2 - t_1)$, where $\hat{\phi}_f$ is the Fourier transform coefficient of the pressure perturbation at frequency f, t_2 is the end of the sampling time, and t_1 is the start of the sampling time]. The sampling rate is 1.0×10^3, and a total of 18,000 samples splitting into four blocks are used to generate the result. The resulting frequency resolution is about 0.22. The spectra show the broadband characteristic of the slat cove flow and the acoustic power cluster in the frequency range of 2.0 to 8.0, which corresponds to $St = 1.2$ to 4.8 (for which the Strouhal number $St = fC_s/u_\infty$ is based on the freestream velocity u_∞ and the chord of the slat C_s). This result agrees with previously reported measurements [38]. The sound pressure level (SPL) against frequency at monitor position 3 (0.2, −0.5, 0.024) is plotted in Fig. 15 to show the spectrum of the acoustic signal in LES calculation. The broadband spectrum has a lump between the frequency of 2.0 and 8.0, indicating the noise is generated by the unsteadiness in the slat cove, and the frequency range of the noise peak agrees with the measurements of Khorrami et al. [11]. The narrowband decay is confined to a range between f^{-2} and f^{-3}, which agrees with the measurements of Choudhari et al. [39] and the computation results of Ewert and Emunds [17].

B. Near-Field Sound Propagation and Far-Field Noise Radiation

With the noise source $\mathbf{q}_m = -(\omega \times \mathbf{u})'$ calculated from the LES, the APE is solved to examine the broadband slat noise attenuation performance of the acoustic liner treatment inside the slat gap. Although it was claimed that the APE-4 system is stable for an arbitrary mean flow [19], noise propagation calculations with the mean flow of the high-lift configuration produce instabilities due to the strong shear layer near the slat trailing edge. As a result, all the APE results shown in this section are obtained with a uniform background flow, and the time-domain impedance boundary condition used in this work models the noise attenuation effect of acoustic liners with the assumption that the presence of the liners has no effect on the flowfield. The APE computations are also used to provide input to integral solutions of the FW–H equation to estimate the far-field noise radiation.

1. *Computation Setup*

A 3-D grid for APE computation is generated by uniformly extruding a basic 2-D grid along the spanwise z direction. The basic 2-D grid consists of 94 blocks with a total of 46,904 nodes, and the total computational domain ranges from -1.75 to $1.75C$ in both the x and the y directions (Fig. 16). The grids are designed to ensure an equivalent grid resolution of at least 7 points per wavelength in the wave propagation direction for a wave frequency of up to 12. As in the LES grid, a total of 26 grid points are used in a spanwise direction, yielding a total of 1.2 million points. The grid near the slat cove region is shown in Fig. 17.

The acoustic fields of three cases are studied in this work: 1) hard wall, 2) slat cove surface lined only, and 3) slat cove surface and leading edge of the lined main element. The slat cove liner starts from the cusp of the slat, but at the slat trailing edge, the available depth is too small to apply a practical liner; the liner treatment is therefore only extended to a position for which at least 12.5×10^{-3} depth is available. The liner covers 56% of the total slat cove surface length. For the liner on the main element, on the basis that the acoustic liner on the main element should avoid the leading edge stagnation point to minimize any possible aerodynamic penalty, the liner is started from a position on the suction surface at a distance of 0.01 from the leading edge and is extended for a distance (which will be covered by slat when the slat is retracted). The positions of the liners are shown in Fig. 17.

The measured liner reactance value given by Motsinger and Kraft [40] is used in the calculation and (in order to achieve attenuation in a wide frequency band) the liner resistance is chosen as 1.0. To model the liner impedance in the time-domain impedance boundary

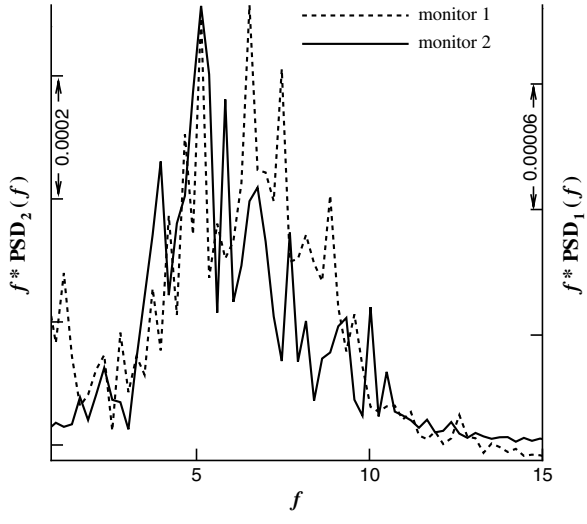

Fig. 14 Frequency spectra at different monitor points.

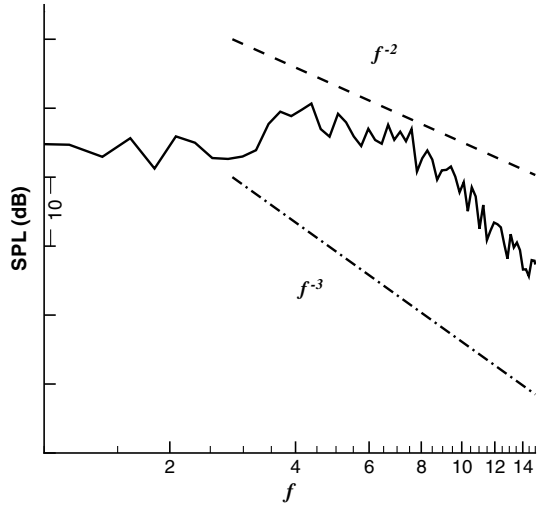

Fig. 15 SPL at monitor position 3 (0.2, −0.5, 0.024).

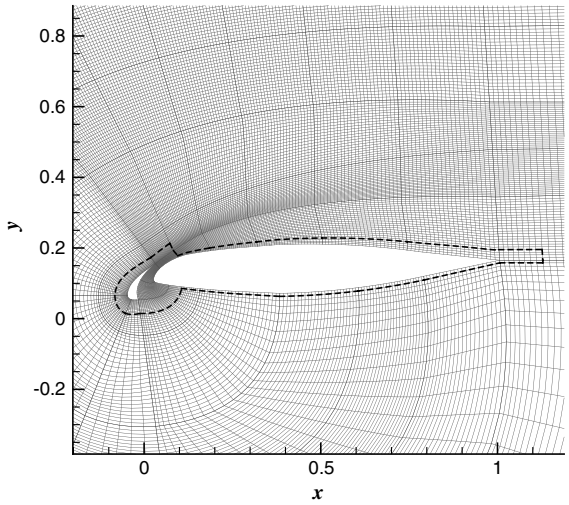

Fig. 16 Cross-sectional view of the 3-D APE grid; the dashed line shows the permeable integration surface used in the FW–H calculation.

condition, a three-parameter model is used, which can be written as

$$Z(\omega) = R + iX = R + i(X_{-1}/\omega + X_1\omega) \tag{7}$$

where X_1 and X_{-1} are the acoustic mass and stiffness used to fit the liner reactance value. Using this model, if $X_1 > 0$ and $X_{-1} < 0$, then the impedance boundary will be stable. In the calculation, the X_1 is 0.0511 and the X_{-1} is −39.627.

The liner treatment is modeled by a time-domain impedance boundary [20] and the slip wall is modeled using a high-order wall boundary condition [41]. An explicit form of buffer zone boundary conditions [32] is used as the nonreflecting boundary condition, and a periodic boundary condition is used in the spanwise direction. The uniform background mean flow with the freestream Mach number of 0.2 and the main element AOA of 12 deg are used in the computations.

The time step size for the computation is $0.0004C/c_\infty$, corresponding to a CFL number of 0.65. The time step corresponds to a sampling frequency of 1.0625 MHz. The calculations are performed for 10 nondimensional time units for each case. The computation is performed on a Linux cluster using 12 2.2 GHz AMD Opterons CPUs, and the CPU cost per time step is 1.25 s.

Both the LES and APE grids have 26 points in the spanwise direction, and the acoustic sources on each $z =$ constant plane are interpolated from the LES grid to the APE grid using Tecplot's [42] inverse distance interpolation function with the options set as a minimum distance of 0, an exponent parameter of 3.5, and the number of closest points selected by the coordinate system as 13. The source terms on the LES grid are recorded every $0.01C/c_\infty$, which corresponds to 25 time steps of the APE computations. The source terms on every 25th time step are read from the recorded file, and the source terms between every 25th time step are linearly interpolated into the APE computations.

3-D integral solutions of the FW–H equation are obtained to compare the far-field acoustic signals for the three cases. An integration surface enclosing all of the high-lift configuration is used for both the LES case and the APE cases, as shown in Fig. 16. The uniform mean flow with a Mach number of 0.2 is used in the FW–H calculation, and a total of 180 far-field observers are positioned on the $z = 0.025$ plane on a circle with a radius of 12.5 from the trailing edge of the slat.

2. *Acoustic Field and Liner Performance*

The source-driven acoustic pressure fields with the hard wall, the slat lined, and the slat and main element lined conditions are shown in Figs. 18–20. The acoustic pressure fields show the broadband characteristics of the slat noise and the noise attenuation effect of acoustic liners.

To quantitatively compare the results of LES and source-driven APE, the far-field directivity results obtained by solving FW–H are given in Fig. 21, in which the sound pressures of different observers are given, and the observer angle is 0 deg in the x direction and increases in the anticlockwise direction.

It should be noted that the APE source terms in Eq. (3) are obtained by neglecting the viscous and entropy sources with the assumption that the neglected terms have no considerable far-field contribution. However, these neglected terms could have an impact on the near-field flow variables, especially on the source region. Therefore, the integration surface of FW–H has to be placed carefully to obtain accurate far-field results. The SPLs on a circle with a radius of 1.25 are directly calculated by solving the APE for the hard wall case, and they are compared with the far-field SPLs calculated by solving the FW–H equation on the observer circle with a radius of 12.5 (in Fig. 21), in which the directly calculated results are scaled for easy comparison. Except for the region with an observer angle larger than 270 deg, in which the APE grid is relatively coarse, a generally good match gives the confidence to the FW–H-predicted far-field results.

By examining the hard wall results of the LES and the source-driven APE, it can be observed that they agree well in general, and the discrepancy is less than 2 dB for most of the observation angles. For the LES results, the two radiation peaks are around 130 and 300 deg. It should be noted that the first radiation peak for the APE results is shifted to nearly 90 deg, which is at least partly due to the mean flow

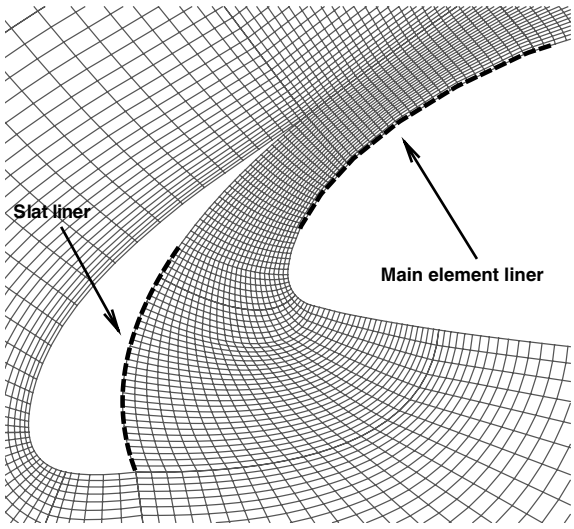

Fig. 17 A view of the APE grid near the slat.

Fig. 18 The acoustic pressure field solved by the source-driven APE with a hard wall condition.

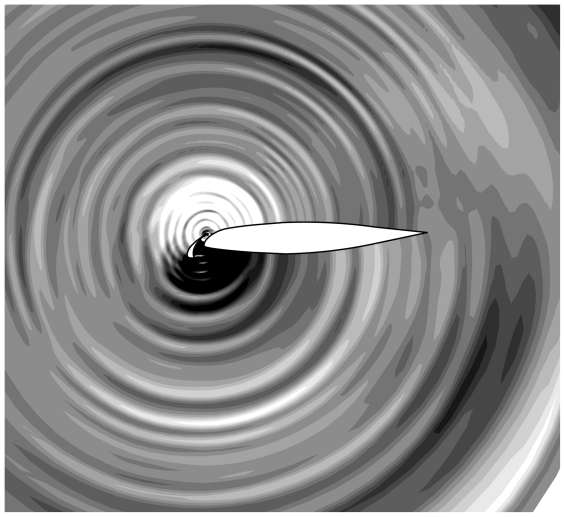

Fig. 19 The acoustic pressure field solved by the source-driven APE with the slat lined condition.

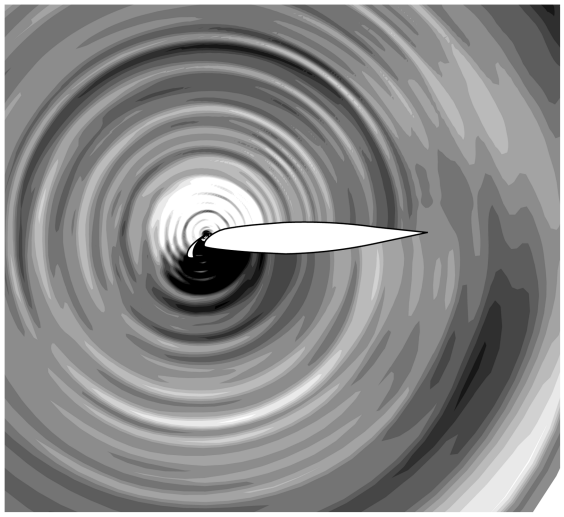

Fig. 20 The acoustic pressure field solved by the source-driven APE with both the slat cove and the main element lined condition.

effect in the LES calculation. The lined cases show the noise attenuation for most of the observation angles. It is not surprising that, when the slat cove and the main element are both lined, the liners performed better than the slat lined case. For the most interested

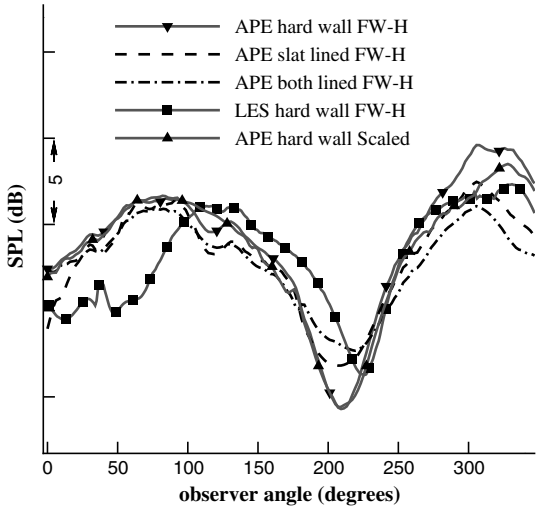

Fig. 21 Comparison of the far-field directivity results of the LES and the source-driven APE.

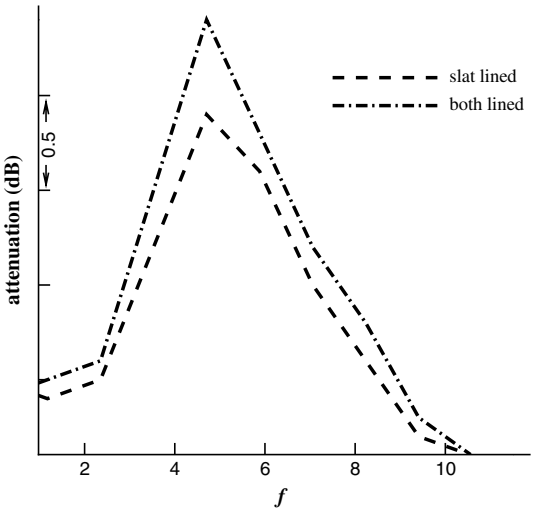

Fig. 22 The averaged attenuation along the frequency.

angle range of 220 to 340 deg, in which the noise propagation is directed toward the ground, the liners show encouraging results, which give a high level of attenuation of larger than 2 dB for an observer angle larger than 260 deg.

Signal analysis using fast Fourier transform is performed for the acoustic pressure histories obtained at the observer points, and the sampling rate is set at 2.5×10^3. A total of 21,250 samples are used. The samples are split into 10 blocks, and the resulting frequency resolution is about 1.2. Figure 22 shows the noise attenuation effect in narrowband spectra calculated by averaging the values of different observer positions, for which the attenuation is defined as

$$Att = 20\log_{10}\frac{\int_{s_0}^{s_1} |p'_{\mathrm{RMS}}|_{\mathrm{hard}}/|p'_{\mathrm{RMS}}|_{\mathrm{lined}}\,\mathrm{d}s}{\int_{s_0}^{s_1}\mathrm{d}s} \tag{8}$$

where Att stands for the space–averaged attenuation, $|p'_{\mathrm{RMS}}|_{\mathrm{hard}}$ is the RMS acoustic pressure for the hard wall case, and $|p'_{\mathrm{RMS}}|_{\mathrm{lined}}$ is the RMS acoustic pressure for the lined wall case. The distance measured along the observe circle is denoted by s.

The maximum attenuation for the slat lined case is 1.9 dB at the frequency of 4.7, and the maximum attenuation for the slat and main element lined case is 2.4 dB at the frequency of 4.7.

IV. Conclusions

The broadband slat noise generation of a high-lift wing configuration is simulated using LES. Results show the characteristics of the unsteady flow and provide insight into the mechanisms of the broadband noise generation. The LES-calculated noise sources are then used to drive the APE. The APE computations are used to compute the near-field sound propagation around the slat and to provide input to integral solutions of the FW–H equation to estimate the far-field noise radiation. The source-driven APE results agree well with that of the LES in terms of the far-field directivity pattern and the SPL. The broadband noise attenuation effects of the acoustic liner treatment on the slat cove surface and the main element leading edge surface are also investigated by employing time-domain liner boundary conditions in the APE computations. Results of a nonoptimized acoustic liner treatment show that the liner can be used to attenuate broadband noise generated by the slat.

Further optimization of the liner characteristic should lead to better attenuation performance. Although the optimization of acoustic liners for broadband noise attenuation is beyond the scope of this paper, it should be noted that for a given noise propagation distance, the APE calculation requires less than 0.64% of CPU time than is required by LES, which suggests that the LES/APE hybrid method could make the optimization possible.

Acknowledgments

Zhaokai Ma was supported by a studentship from the School of Engineering Sciences, University of Southampton, Southampton, England, U.K.. The authors wish to thank L. C. Chow and N. Molin of Airbus and M. Smith of the Institute of Sound and Vibration Research for their assistance during the project.

References

[1] Agarwal, A., and Morris, P. J., "Investigation of the Physical Mechanisms of Tonal Sound Generation by Slats," 8th AIAA/CEAS Aeroacoustics Conference, AIAA Paper 2002-2575, June 2002.

[2] Khorrami, M. R., Berkman, M. E., and Choudhari, M., "Unsteady Flow Computations of a Slat with a Blunt Trailing Edge," *AIAA Journal*, Vol. 38, No. 11, Nov. 2000, pp. 2050–2058. doi:10.2514/2.892

[3] Olson, S., Thomas, F. O., and Nelson, R. C., "Mechanisms of Slat Noise Production in a 2-D Multi-Element Airfoil Configuration," 7th AIAA/CEAS Aeroacoustics Conference, AIAA Paper 2001-2156, May 2001.

[4] Khorrami, M. R., Choudhari, M. M., Singer, B. A., Lockard, D. P., and Streett, C. L., "In Search of the Physics: The Interplay of Experiment and Computation in Slat Aeroacoustics," 41st Aerospace Sciences Meeting, AIAA Paper 2003-0980, Jan. 2003.

[5] Choudhari, M. M., Lockard, D. P., Macaraeg, M. G., Singer, B. A., Streett, C. L., Neubert, G. R., Stoker, R. W., Underbrink, J. R., Berkman, M. E., Khorrami, M. R., and Sadowski, S. S., "Aeroacoustic Experiments in the Langley Low-Turbulence Pressure Tunnel," NASA TM-2002-211432, Feb. 2002.

[6] Ma, Z., Smith, M., Richards, S. K., and Zhang, X., "Slat Noise Attenuation Using Acoustic Liners," 11th AIAA/CEAS Aeroacoustics Conference, AIAA Paper 2005-3009, May 2005.

[7] Smith, M. G., Chow, L. C., and Molin, N., "Attenuation of Slat Trailing Edge Noise Using Slat Gap Acoustic Liners," AIAA Paper 2006-2666, 2006.

[8] Choudhari, M. M., and Khorrami, M. R., "Slat Cove Unsteadiness: Effect of 3-D Flow Structures," 44th AIAA Aerospace Sciences Meeting and Exhibit, AIAA Paper 2006-0211, Jan. 2006.

[9] Terracol, M., Labourasse, E., Manoha, E., and Sagaut, P., "Simulation of the 3-D Unsteady Flow in a Slat Cove for Noise Prediction," 9th AIAA/CEAS Aeroacoustics Conference, AIAA Paper 2003-3110, May 2003.

[10] Deck, S., "Zonal-Detached-Eddy Simulation of the Flow Around a High-Lift Configuration," *AIAA Journal*, Vol. 43, No. 11, 2005, pp. 2372–2384. doi:10.2514/1.16810

[11] Khorrami, M. R., Singer, B. A., and Lockard, D. P., "Time-Accurate Simulations and Acoustic Analysis of Slat Free-Shear Layer: Part 2," 8th AIAA/CEAS Aeroacoustics Conference, AIAA Paper 2002-2579, June 2002.

[12] Khorrami, M. R., Choudhari, M. M., and Jenkins, L. N., "Characterization of Unsteady Flow Structures Near Leading Edge Slat, Part 2: 2-D Computations," 10th AIAA/CEAS Aeroacoustics Conference, AIAA Paper 2004-2802, May 2004.

[13] Bailly, C., Lafon, P., and Candel, S., "A Stochastic Approach to Compute Noise Generation and Radiation of Free Turbulent Flows," 1st AIAA/CEAS Aeroacoustics Conference, AIAA Paper 1995-092, June 1995.

[14] Bailly, C., Lafon, P., and Candel, S., "Computation of Noise Generation and Propagation for Free and Confined Turbulent Flows," 2nd AIAA/CEAS Aeroacoustics Conference, AIAA Paper 1996-1732, May 1996.

[15] Bailly, C., and Juvé, D., "A Stochastic Approach to Compute Subsonic Noise using Linearized Euler's Equations," 5th AIAA/CEAS Aeroacoustics Conference, AIAA Paper 1999-1872, May 1999.

[16] Ewert, R., and Bauer, M., "Towards the Prediction of Broadband Trailing Edge Noise Via Stochastic Surface Sources," 10th AIAA/CEAS Aeroacoustics Conference, AIAA Paper 2004-2861, 2004.

[17] Ewert, R., and Emunds, R., "CAA Slat Noise Studies Applying Stochastic Sound Sources Based on Solenoidal Digital Filters," 11th AIAA/CEAS Aeroacoustics Conference, AIAA Paper 2005-2862, 2005.

[18] Agarwal, A., and Morris, P. J., "Prediction Method for Broadband Noise from Unsteady Flow in a Slat Cove," *AIAA Journal*, Vol. 44, No. 2, 2006, pp. 301–310. doi:10.2514/1.12991

[19] Ewert, R., and Schröder, W., "Acoustic Perturbation Equations Based on Flow Decomposition Via Source Filtering," *Journal of Computational Physics*, Vol. 188, No. 2, 2003, pp. 365–398. doi:10.1016/S0021-9991(03)00168-2

[20] Fung, K.-Y., Ju, H., and Tallapragada, B., "Impedance and Its Time-Domain Extensions," *AIAA Journal*, Vol. 38, No. 1, Jan. 2000, pp. 30–38. doi:10.2514/2.950

[21] Brentner, K. S., "Prediction of Helicopter Discrete Frequency Rotor Noise: A Computer Program Incorporation Realistic Blade Motions and Advanced Acoustic Formulation," NASA TM-87721, 1986.

[22] Rizzetta, D. P., Visbal, M. R., and Blaisdell, G. A., "A Time-Implicit High-Order Compact Differencing and Filtering Scheme for Large-Eddy Simulation," *International Journal of Numerical Methods in Fluids*, Vol. 42, No. 6, 2003, pp. 665–693. doi:10.1002/fld.551

[23] Smagorinsky, J. S., "General Circulation Experiments with the Primitive Equations," *Monthly Weather Review*, Vol. 91, No. 3, 1963, pp. 99–165. doi:10.1175/1520-0493(1963)091<0099:GCEWTP>2.3.CO;2

[24] Jameson, A., "Time Dependent Calculations Using Multigrid with Applications to Unsteady Flows Past Airfoils and Wings," 10th Computational Fluid Dynamics Conference, AIAA Paper 1991-1956, June 1991.

[25] Hixon, R., "Prefactored Small-Stencil Compact Schemes," *Journal of Computational Physics*, Vol. 165, No. 2, 2000, pp. 522–541. doi:10.1006/jcph.2000.6631

[26] Kennedy, C. A., and Carpenter, M. H., "Comparison of Several Numerical Methods for Simulation of Compressible Shear Layers," NASA TP-2446, 1997.

[27] Visbal, M. R., and Rizzetta, D. P., "Large-Eddy Simulation on Curvilinear Grids using Compact Differencing and Filtering Schemes," *Journal of Fluids Engineering*, Vol. 124, No. 4, 2002, pp. 836–847. doi:10.1115/1.1517564

[28] Ma, Z., "Numerical Investigation of Slat Noise Attenuation Using Acoustic Liners," Ph.D. Thesis, University of Southampton, Southampton, England, U.K., 2008.

[29] Ashcroft, G., and Zhang, X., "Optimized Prefactored Compact Schemes," *Journal of Computational Physics*, Vol. 190, No. 2, 2003, pp. 459–477. doi:10.1016/S0021-9991(03)00293-6

[30] Hu, F. Q., Hussaini, M. Y., and Manthey, J. L., "Low-Dissipation and Low-Dispersion Runge–Kutta Schemes for Computational Acoustics," *Journal of Computational Physics*, Vol. 124, No. 1, 1996, pp. 177–191. doi:10.1006/jcph.1996.0052

[31] Spalart, P. R., "Young-Person's Guide to Detached Eddy Simulation Grids," NASA CR-2001-211032, July 2001.

[32] Wasistho, B., Guerts, B. J., and Kuerten, J. G. M., "Simulation Techniques for Spatially Evolving Instabilities in Compressible Flow Over a Flat Plate," *Computers and Fluids*, Vol. 26, No. 7, 1997, pp. 713–739. doi:10.1016/S0045-7930(97)00021-2

[33] Delcayre, F., and Dubief, Y., "On Coherent-Vortex Identification in Turbulence," *Journal of Turbulence*, Vol. 1, No. 11, 2000, pp. 1–22. doi:10.1088/1468-5248/1/1/011

[34] Woodward, D. S., and Lean, D. E., "Where Is High-Lift Today: A Review of Past UK Research Programmes," *AGARD Conference Proceedings 515: High-Lift System Aerodynamics*, CP515, AGARD, Sept. 1993, Chap. 1, pp. 1–37.

[35] Takeda, K., Ashcroft, G. B., Zhang, X., and Nelson, P. A., "Unsteady Aerodynamics of Slat Cove Flow in a High-Lift Device Configuration," 39th Aerospace Sciences Meeting, AIAA Paper 2001-0706, Jan. 2001.

[36] Paschal, K. B., Jenkins, L., and Yao, C.-S., "Unsteady Slat Wake Characteristics of a 2-D High-Lift Configuration," 38th Aerospace Sciences Meeting, AIAA Paper 2000-0139, Jan, 2000.

[37] Jenkins, L. N., Khorrami, M. R., and Choudhari, M., "Characterization of Unsteady Flow Structures Near Leading-Edge Slat, Part 1: PIV Measurements," 10th AIAA/CEAS Aeroacoustics Conference, AIAA Paper 2004-2801, May 2004.

[38] Dobrzynski, W., and Pott-Pollenske, M., "Slat Noise Source Studies for Farfield Noise Prediction," 7th AIAA/CEAS Aeroacoustics Conference, AIAA Paper 2001-2158, May 2001.

[39] Choudhari, M., Khorrami, M. R., Lockard, D. P., Atkins, H., and Lilley, G., "Slat Cove Noise Modeling: A Posteriori Analysis of Unsteady RANS Simulations," 8th AIAA/CEAS Aeroacoustics Conference, AIAA Paper 2002-2468, June 2002.

[40] Motsinger, R. E., and Kraft, R. E., "Design and Performance of Duct Acoustic Treatment," *Aeroacoustics of Flight Vehicles: Theory and Practice*, Vol. 2: Noise Control, NASA RP-1258, TR 90-3052, 1991, p. 184.

[41] Hixon, R., "Curvilinear Wall Boundary Conditions for Computational Aeroacoustics," AIAA Paper 1999-2539, 1999.

[42] Tecplot, Software Package, Ver. 9.0, Tecplot, Inc., Bellevue, WA, 2002.

D. Gaitonde
Associate Editor